HHS Public Access

Author manuscript

Cell Rep. Author manuscript; available in PMC 2021 January 06.

Published in final edited form as:

Cell Rep. 2020 December 29; 33(13): 108570. doi:10.1016/j.celrep.2020.108570.

An Additional Ca^{2+} Binding Site Allosterically Controls TMEM16A Activation

Son C. Le[1], **Huanghe Yang**[1,2,3,*]

[1]Department of Biochemistry, Duke University School of Medicine, Durham, NC 27710, USA

[2]Department of Neurobiology, Duke University School of Medicine, Durham, NC 27710, USA

[3]Lead Contact

SUMMARY

Calcium (Ca^{2+}) is the primary stimulus for transmembrane protein 16 (TMEM16) Ca^{2+}-activated chloride channels and phospholipid scramblases, which regulate important physiological processes ranging from smooth muscle contraction to blood coagulation and tumor progression. Binding of intracellular Ca^{2+} to two highly conserved orthosteric binding sites in transmembrane helices (TMs) 6–8 efficiently opens the permeation pathway formed by TMs 3–7. Recent structures of TMEM16K and TMEM16F scramblases revealed an additional Ca^{2+} binding site between TM2 and TM10, whose functional relevance remains unknown. Here, we report that Ca^{2+} binds with high affinity to the equivalent third Ca^{2+} site in TMEM16A to enhance channel activation. Our cadmium (Cd^{2+}) metal bridging experiments reveal that the third Ca^{2+} site's conformational states can profoundly influence TMEM16A's opening. Our study thus confirms the existence of a third Ca^{2+} site in TMEM16A, defines its functional importance in channel gating, and provides insight into a long-range allosteric gating mechanism of TMEM16 channels and scramblases.

Graphical Abstract

*Correspondence: huanghe.yang@duke.edu.

AUTHOR CONTRIBUTIONS

H.Y. and S.C.L. conceived and designed the study. H.Y. supervised the project. S.C.L. performed all experiments and data analysis. S.C.L. and H.Y. wrote the manuscript.

DECLARATION OF INTERESTS

The authors declare no competing interests.

SUPPLEMENTAL INFORMATION

Supplemental Information can be found online at https://doi.org/10.1016/j.celrep.2020.108570.

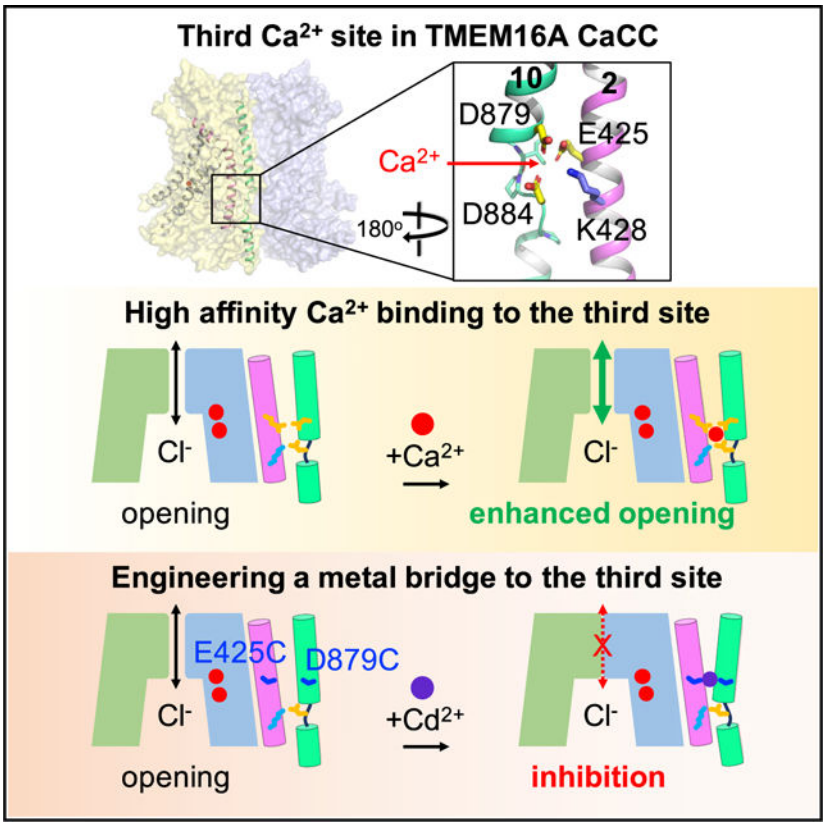

In Brief

Le and Yang present electrophysiological evidence for a third Ca^{2+} binding site in the Ca^{2+}-activated chloride channel TMEM16A. They show that Ca^{2+} binds with high affinity to this site to facilitate channel opening, providing insight into an allosteric gating mechanism in TMEM16 ion channels and scramblases.

INTRODUCTION

Transmembrane protein 16A (TMEM16A) belongs to the TMEM16 family whose members include both Ca^{2+}-activated chloride channels (CaCCs) (Caputo et al., 2008; Schroeder et al., 2008; Yang et al., 2008) and dual functional Ca^{2+}-activated non-selective ion channels and phospholipid scramblases (Bushell et al., 2019; Le et al., 2019b; Malvezzi et al., 2013; Suzuki et al., 2010, Suzuki et al., 2013; Yang et al., 2012). The CaCC TMEM16A plays an important role in regulating smooth muscle contraction, gut motility, fluid secretion, nociception, and anxiety (Cho et al., 2020; Scudieri et al., 2012; Whitlock and Hartzell, 2017). Abnormal expression of TMEM16A is intimately associated with numerous types of cancers, such as gastrointestinal stromal tumors; head and neck squamous carcinomas; and breast, pancreatic, and prostate cancer, thus highlighting its potential as a biomarker and promising anticancer therapeutic target (Crottès and Jan, 2019).

As a polymodal sensor, the gating landscape of TMEM16A is shaped by the synergistic action of Ca^{2+} binding and membrane depolarization, both of which promote channel

opening (Falzone et al., 2018; Whitlock and Hartzell, 2017). TMEM16A's channel activity is also positively regulated by the phosphatidylinositol (4,5)-bisphosphate (PIP_2) (De Jesús-Pérez et al., 2018; Le et al., 2019a; Ta et al., 2017; Tembo et al., 2019; Yu et al., 2019). Extensive structural and functional studies have advanced our mechanistic understanding of TMEM16A's Cl^- permeation, Ca^{2+}-dependent gating, and its regulation by lipids. Assembled as a homodimer, each TMEM16A subunit contains 10 membrane-spanning segments with its own independent pore (Figure 1A) (Dang et al., 2017; Jeng et al., 2016; Lim et al., 2016; Paulino et al., 2017a; Paulino et al., 2017b). Transmembrane helix (TM)3–TM8 form the pore-gate domain that is essential for ion permeation, Ca^{2+} sensing, and PIP_2 regulation, whereas TMs 1, 2, 9, and 10 form the supporting domain that establishes the dimer interface (Le et al., 2019a). The hourglass-shaped permeation pathway is composed of residues from TM3 to TM7, many of which have been implicated in controlling anion selectivity (Dang et al., 2017; Peters et al., 2015; Yang et al., 2012). Binding of intracellular Ca^{2+} to five highly conserved acidic residues and an asparagine from TM6–TM8 (Figure 1A) (Brunner et al., 2014; Paulino et al., 2017a; Tien et al., 2014; Yu et al., 2012) not only induces a prominent conformational rearrangement of TM6 to help open the steric gate but also relieves a second, electrostatic gate imposed by the Ca^{2+}-binding acidic residues, subsequently allowing chloride conduction (Dang et al., 2017; Lam and Dutzler, 2018; Paulino et al., 2017a; Peters et al., 2018).

Intriguingly, recent structural studies of TMEM16F and TMEM16K scramblases have revealed yet another Ca^{2+} binding site in TM2 and TM10 of the supporting domain (Figures 1D–1F) (Alvadia et al., 2019; Bushell et al., 2019). We refer to this additional Ca^{2+} site as the "third Ca^{2+} site" to distinguish it from the primary "orthosteric sites" in TM6–TM8. Despite not being resolved initially, it was later suggested that the Ca^{2+}-bound TMEM16A structure (Paulino et al., 2017a) also harbors an electron density at the equivalent site, presumably deriving from a bound Ca^{2+} ion (Alvadia et al., 2019). This assumption is supported by the fact that the Ca^{2+}-coordinating residues at the third site are highly conserved among TMEM16 proteins (Figure 1D). More importantly, the distant location of this Ca^{2+} site from the pore-gate domain (Figures 1A–1C) also suggests that TMEM16 proteins may undergo a long-range allosteric modulation, a regulatory mechanism common in many ion channels and membrane receptor proteins that harbor multiple topologically distinct, yet tightly coupled, sensors (Changeux and Christopoulos, 2016). Nevertheless, lack of functional evidence raises questions on the existence and functional relevance of this Ca^{2+} site in regulating TMEM16 proteins. Interestingly, a missense mutation of a third Ca^{2+}-coordinating residue, D615N, in TMEM16K was identified in a spinocerebellar ataxia type 10 (SCAR10) patient with unknown patho-physiology (Figures 1D–1F) (Balreira et al., 2014). Therefore, understanding the functional role of this third Ca^{2+} binding site not only informs an allosteric gating mechanism of TMEM16 proteins but also provides potential insight into the molecular patho-physiology of TMEM16K variant in SCAR10.

To define the functional existence and the molecular basis for channel-gating modulation by the third Ca^{2+} binding site, we studied the TMEM16A CaCC using electrophysiology, mutagenesis, and Cd^{2+}-mediated metal bridging. Here, we show that the third site in TM2 and TM10 binds intracellular Ca^{2+} with high affinity. Notably, mutating the Ca^{2+}-binding residues at this site not only significantly reduces its Ca^{2+} sensing but also directly affects

the channel's activation gate. Using Cd^{2+}-mediated metal bridging of cysteines engineered to the third Ca^{2+} site, we further demonstrate that the conformational states of TM2 and TM10 can strongly influence TMEM16A's channel opening in a manner that is independent of the orthosteric Ca^{2+} sites. Our functional analyses thus unveil an unknown regulatory mechanism in which channel activation is facilitated by Ca^{2+} binding to the TM2–TM10 site. We anticipate that our present findings could stimulate future mechanistic investigations on the allosteric regulation and the development of allosteric modulators for TMEM16 ion channels and phospholipid scramblases.

RESULTS

Mutation of the Putative Third Ca^{2+} Site Residues Alters TMEM16A's Ca^{2+} Sensing

Given the structural and sequence conservation between mammalian TMEM16 proteins at the putative third Ca^{2+} binding site (Figures 1A and 1D–1F), we examined whether the equivalent site in TMEM16A contributes to channel gating by measuring the Ca^{2+}-dependent activation of the alanine mutations of E425 and K428 from TM2 and of D879 and D884 from TM10 (Figures 2A–2E). Paradoxically, the K428A and D884A mutations markedly reduce, while E425A and D879A enhance, the apparent Ca^{2+} sensitivity of TMEM16A (Figures 2F and 2I; Table S1). Similar phenotypes were also observed in the charge-reversing mutations of these residues (Figure S1; Table S1). Although they do not tell us whether the third Ca^{2+} site residues indeed bind Ca^{2+}, these results offer clear evidence to support that this putative Ca^{2+} site in TM2 and TM10 significantly impacts the Ca^{2+}-dependent activation of TMEM16A.

TMEM16A's D884 residue is absolutely conserved among mammalian TMEM16 proteins and corresponds to TMEM16K D615, whose D615N variant was identified in a patient with autosomal recessive SCAR10 (Figures 1A, 1D, and 1F) (Balreira et al., 2014; Bushell et al., 2019). To gain some insight into the mutational effect of TMEM16K D615N, we measured the Ca^{2+} sensitivity of the equivalent TMEM16A D884N mutant (Figure 2G). Similar to D884A, the D884N mutation also significantly reduces TMEM16A Ca^{2+} sensitivity, albeit to a lesser extent (Figures 2H and 2I; Table S1). Although this observation implies a possibility that D615N also impairs TMEM16K's function, the previous study by Bushell et al. (2019) found that this mutant displayed no obvious defects in its lipid scrambling under both Ca^{2+}-free and saturating Ca^{2+} conditions using reconstituted liposomes. We speculated that the mutational effect of TMEM16K D615N may require a more rigorous assessment of its Ca^{2+} dose-dependent lipid scrambling, especially considering the relatively lower sensitivity/resolution of lipid scrambling assays compared to that of electrophysiology as well as the less disruptive Asp-to-Asn substitution.

Taken together, our single point mutation characterizations of TMEM16A reveal that disrupting the putative third Ca^{2+} binding site in TM2 and TM10 alters channel activation.

Disrupting the Third Ca^{2+} Site Residues Alters Channel Activation independent of Ca^{2+}

Considering the pronounced effects from the alanine and charge-reversing mutations of the third Ca^{2+} site on channel activation, we speculated that such perturbations could either

affect the orthosteric-site-mediated, Ca^{2+}-dependent gating or modulate the channel's activation gate independent of Ca^{2+}. To test whether disrupting the third Ca^{2+} site residues would remotely impact TMEM16A's activation gate in the pore-gate domain independent of Ca^{2+} binding, we utilized the gain-of-function mutant Q645A (Peters et al., 2018), which allows us to measure TMEM16A's channel activation in the complete absence of Ca^{2+} (Figure 3A). To accurately quantify their voltage-dependent activation, we normalized the measured conductance in the absence of Ca^{2+} to the maximal conductance (G_{max}), which was obtained by exposing the excised membrane patches to saturating 100 μM Ca^{2+} (Figure 3A). Interestingly, alanine mutations of the putative third Ca^{2+} site residues in the Q645A background markedly shift the conductance-voltage (G-V) curves in the absence of Ca^{2+} (Figures 4B–4F). Whereas E425A and D879A enhance channel activation and shift the G-V curve toward more a negative voltage range, K428A and D884A shift it toward more positive voltages. Furthermore, the charge-reversing mutants E425K and D879K also promote, whereas K428E and D884K reduce, TMEM16A's channel activation in the absence of Ca^{2+} (Figure S2). The G/G_{max}-V curves of these mutant channels did not go beyond 0.5 (Figure 3F), which prevents us from extrapolating the half-maximal activation voltage ($V_{1/2}$) values for further comparisons. Nonetheless, the mutational effects of the third Ca^{2+} site residues on TMEM16A's Ca^{2+}-independent activation strikingly mirror their respective effects on the channel's Ca^{2+}-dependent activation seen in the wild-type (WT) background (Figure 2; Figure S1). Because the orthosteric Ca^{2+} sites in TM6–TM8 account for the measured Ca^{2+}-dependent currents in the WT background (Figure 2), the observed alterations of TMEM16A's Ca^{2+} sensitivity from the third site mutations should arise from their Ca^{2+}-independent allosteric effects on channel gating. Therefore, the paradoxical effects of the third Ca^{2+} site mutants on WT TMEM16A's Ca^{2+} sensitivity (Figures 2A–2F) likely reflect a net result of the Ca^{2+}-dependent activation by the orthosteric Ca^{2+} sites and the Ca^{2+}-independent allosteric effects from perturbation of the third Ca^{2+} site on the channel's activation gate.

The Putative Third Ca^{2+} Site in TM2 and TM10 Binds Ca^{2+}

Because neutralizing the orthosteric Ca^{2+} binding residues severely diminishes Ca^{2+}-dependent activation in TMEM16A (Tien et al., 2014; Yu et al., 2012), it is thus intriguing that neutralizing E425A and D879A mutants at the third Ca^{2+} site enhance, whereas K428A and D884A decrease, the apparent Ca^{2+} sensitivity of TMEM16A (Figure 2I; Table S1). However, the fact that these mutants are sufficient to sensitize or attenuate channel activation in the absence of Ca^{2+} binding is suggestive of their potential pleiotropic effects on not only the channel's activation gate (Figure 3; Figure S2) but also Ca^{2+} binding to this third site. We reasoned that the mutational effects on channel activation from disrupting the third Ca^{2+} site residues could be confounded by the intact orthosteric Ca^{2+} sites. Thus, to specifically investigate the Ca^{2+} binding properties of the third site, we utilized the E701K and D734R mutations, two charge-reversing mutations of the Ca^{2+}-coordinating E701 and D734 on TM7 and TM8, respectively (Figure 1A), previously shown to abolish Ca^{2+} binding to the orthosteric Ca^{2+} sites (Tien et al., 2014; Yu et al., 2012) (Figure 4A). We also introduced the Q645A mutation on TM6 to allow the channel to adopt a partially released steric gate that can be opened via membrane depolarization (Lam and Dutzler, 2018; Peters et al., 2018). Remarkably, the resulting triple mutant Q645A/E701K/D734R (henceforth referred to as

QA/EK/DR) channels display robust Ca^{2+} sensitivity, as Ca^{2+} application strongly potentiates the basal current mediated by Q645A (Figure 4B).

Because the E701K and D734R mutations abolish Ca^{2+} binding to the orthosteric sites, we attributed the observed Ca^{2+} sensing capability of QA/EK/DR to the third Ca^{2+} site in TM2–TM10 due to the following lines of evidence. First, by analyzing the Ca^{2+}-sensitive currents, which were obtained by subtracting the basal current from each Ca^{2+}-elicited steady-state current (Figure 4B), we found that the third Ca^{2+} site has an estimated Ca^{2+} half-maximal activation concentration (EC_{50}) of ~320 nM ± 10 nM (Figures 4G–4I; Table S1), which is well within physiological range and is thus unlikely to be mediated by the already impaired orthosteric sites. To rule out any potential confounding effects from Ca^{2+}-dependent rundown on our Ca^{2+} EC_{50} analysis, we performed rundown-corrected measurements of the QA/EK/DR mutant and obtained a comparable Ca^{2+} EC_{50} value of ~360 nM ± 20 nM (Figures S3A–S3C; Table S1). Second, consistent with its location closer to the cytosolic side, the Ca^{2+} sensitivity of the third site shows no apparent voltage dependence (Figures S3D–S3F; Table S1), which is distinct from the highly voltage-dependent Ca^{2+} sensitivity of the orthosteric Ca^{2+} binding sites, owing to their location deep into the membrane field (Dang et al., 2017; Paulino et al., 2017a; Xiao et al., 2011). Finally, we designed single alanine mutations of the third Ca^{2+} site—E425A, K428A, D879A and D884A—in the context of the QA/EK/DR background, examined their Ca^{2+} sensitivity, and found that they substantially reduce the Ca^{2+}-dependent currents of the QA/EK/DR channels (Figures 4C–4F). The reduced Ca^{2+}-dependent currents are not due to decreased channel expression, as these quadruple mutants display robust channel activation in the absence of Ca^{2+} (Figures S4A–S4F, S4M, and S4N). Notably, alanine mutations of the three acidic residues, E425, D879, and D884, most dramatically attenuate the third site's Ca^{2+} sensing, whereas that of the basic K428 residue causes a less pronounced reduction, consistent with the potential structural role of K428 in stabilizing the third Ca^{2+} site (Figures 4G–4I). Our observation that E425A and D884A strongly reduce the Ca^{2+} sensitivity of the third site is particularly fascinating in light of the recent structural studies showing that the equivalent E395-D859 and E259-D615 residues in TMEM16F and TMEM16K, respectively, directly coordinate the bound third Ca^{2+} ion via their side-chain carboxylates (Alvadia et al., 2019; Bushell et al., 2019). Taken together, our characterizations of the third Ca^{2+} site on the QA/EK/DR background demonstrate that Ca^{2+} binds to this site with high affinity to promote channel opening.

Charged Residues at the Third Ca^{2+} Site Play Differential Roles in Ca^{2+} Binding

To further explore the functional roles of the third Ca^{2+} site residues, we carried out Ca^{2+}-dependent current measurements of all six combinations of double mutants at the third Ca^{2+} site on the QA/EK/DR background. Provided the strongly reduced Ca^{2+} sensitivity by single alanine mutations of E425, D879, and D884 (Figures 4G–4I), we reasoned that double-mutant variants comprising two acidic residues at the third site should abolish its Ca^{2+} binding. In agreement with this hypothesis, we found that the acidic double mutants E425A/D879A, E425A/D884A, and D879A/D884A completely lose their Ca^{2+} sensing capability (Figures 5A, 5B, and 5E). The loss of Ca^{2+} sensitivity by the basic/acidic E425A/K428A double mutant further highlights the importance of E425 at the third Ca^{2+} site (Figure 5E). It

is worth noting that the lack of Ca^{2+} sensing by these mutants is not due to impaired membrane trafficking, as evidenced by their robust membrane expression (Figure S4Q) and voltage-dependent channel activation in the absence of Ca^{2+} (Figures S4G–S4L, S4O, and S4P). By contrast, the basic/acidic double mutants K428A/D879A and K428A/D884A exhibit an apparent Ca^{2+} sensitivity comparable to that of D879A and D884A, respectively (Figures 5C–5F; Table S1). The observation that neutralizing two acidic residues completely extinguishes its Ca^{2+} sensing further strengthens our conclusion that the third site binds Ca^{2+} to facilitate channel opening.

The ability of K428A/D879A and K428A/D884A double mutants to retain some Ca^{2+} sensitivity (Figures 5C–5E; Table S1) allowed us to conduct double-mutant cycle analysis (Hidalgo and MacKinnon, 1995) to study the potential coupling between these charged residues (Figures 5F, 5G, and 5I). Interestingly, our analyses reveal that K428 is energetically coupled to D879 and to D884 with a significant energy of interaction ($\Delta\Delta G_{int}$) of -1.07 ± 0.03 kcal $\cdot$ mol^{-1} and -0.98 ± 0.02 kcal $\cdot$ mol^{-1}, respectively (Figures 5H and 5J). This suggests that, although K428 is unlikely to directly coordinate Ca^{2+}, its energetically favorable interactions with D879 and D884 may serve an important structural role in stabilizing these first-shell acidic residues for Ca^{2+} binding.

Taken together, in excellent agreement with previous structural studies (Alvadia et al., 2019; Bushell et al., 2019; Paulino et al., 2017a), our functional analyses not only validate that Ca^{2+}, indeed, binds to the third site in TM2 and TM10 but also unveil the distinct roles of its charged residues in mediating Ca^{2+} binding and regulating channel activation.

TM2-TM10 Interaction Can Strongly Influence TMEM16A's Channel Gating

The multifaceted role of the third site in modulating TMEM16A's Ca^{2+}-dependent and Ca^{2+}-independent channel activation prompted us to speculate that the conformation of TM2 and TM10 at this region may be key to allosterically controlling channel gating. To test this hypothesis, we performed double-cysteine substitutions to the third Ca^{2+} site and sought to assess whether the transition metal ion Cd^{2+} could form a metal bridge between TM2 and TM10 and how such restricting their conformation would impact channel activation. The readily reversible formation of Cd^{2+} metal bridge permits temporal probing of the effects from crosslinking TM2 and TM10 on channel activity (Linsdell, 2015). By screening different TM2–TM10 interhelical pairs of cysteines, we found that application of Cd^{2+} (0.5, 1, or 10 μM) largely abolishes channel activity of the double mutant E425C/D879C, but not WT or the single-cysteine mutants E425C and D879C, even under saturating 100 μM Ca^{2+} (Figures 6A–6E). The partial inhibition seen in WT channels is likely caused by Cd^{2+} competing with Ca^{2+} for binding to the orthosteric Ca^{2+} sites, as this inhibition is strongly attenuated by elevating intracellular Ca^{2+} and is rapidly reversed upon Cd^{2+} removal (Figures 6A and 6F; Figure S5). In stark contrast, Cd^{2+}-mediated inhibition of E425C/D879C is much longer lasting, as evidenced by the slow current recovery rate (Figure 6F), which is indicative of a high-affinity Cd^{2+}-E425C/D879C metal bridge. In fact, we found that Cd^{2+} also potently inhibits the double mutant E425H/D879C (Figures S6A, S6D and S6E), in accordance with the ability of Cd^{2+} to bridge a histidine and a cysteine (Linsdell, 2015). Cd^{2+} elicits no obvious effects on other TM2–TM10 interhelical double-cysteine

mutants, including E425C/D884C and K428C/D879C (Figures S6B–S6E), presumably owing to a lack of optimal distance and/or orientation for Cd^{2+} metal bridging. The K428C/D884C double mutant shows Ca^{2+}-elicited currents that are too small for analysis (Figure S6F).

We also examined whether the inhibitory effect from chemically restraining TM2 and TM10 is dependent upon Ca^{2+} binding to orthosteric sites. By again exploiting the QA/EK/DR background construct to interrogate the effects of Cd^{2+}-mediated bridging in the absence of Ca^{2+}, we found that 10 μM Cd^{2+} markedly inhibits the voltage-dependent channel activity of E425C/D879C but not the Cd^{2+}-insensitive E428C/D884C mutant (Figure S7). Taken together, these results reveal that altering the conformation of TM2–TM10 at the third Ca^{2+} site by bridging the substituted cysteines E425C and D879C leads to profound channel inhibition in a manner that is independent of Ca^{2+} binding to the orthosteric sites.

DISCUSSION

Here, we present functional evidence to establish that, in addition to the two orthosteric sites in the pore-gate domain, TMEM16A also possesses an additional Ca^{2+} binding site comprising E425 and K428 in TM2 and D879 and D884 in TM10 (Figure 7A). Our data not only consolidate recent structural findings of a third Ca^{2+} binding site in TMEM16F and TMEM16K scramblases (Alvadia et al., 2019; Bushell et al., 2019) but also functionally validate that the unassigned electron density observed in TM2–TM10 of the liganded TMEM16A structure, indeed, represents the third bound Ca^{2+} ion (Paulino et al., 2017a).

Allosteric Modulation of TMEM16A's Gating via an Additional High-Affinity Ca^{2+} Site

In TMEM16 proteins, the pore-gate domain accommodates both the two orthosteric Ca^{2+} sites and the activation gate, thereby allowing Ca^{2+} binding to efficiently open the activation gate (Figures 7A and 7B). This structural arrangement differs from that of the Ca^{2+}-activated large conductance potassium BK channels, whose two Ca^{2+} sensors are distantly located within disparate parts of the cytosolic gating ring and independently control activation via long-range allosteric coupling mechanisms (Hite et al., 2017; Horrigan, 2012; Horrigan and Aldrich, 2002; Tao et al., 2017; Yang et al., 2015; Zhou et al., 2017). Therefore, the presence of an additional Ca^{2+} site that is distant from the pore-gate domain raises the question of whether TMEM16 proteins may also utilize a long-range allosteric mechanism to regulate ion/lipid permeation gating.

To address this question and to understand the relationship between the third Ca^{2+} site and the orthosteric Ca^{2+} sites, we used three different TMEM16A backgrounds: WT, Q645A, and QA/EK/DR. First, our Ca^{2+}-dependent measurements on the WT background revealed the involvement of the third Ca^{2+} site residues in channel activation (Figure 2). Second, the Q645A background allowed us to demonstrate that mutation of the third site residues alters channel activation independent of Ca^{2+} binding to the orthosteric sites, which is in support of a long-range allosteric coupling between this additional Ca^{2+} site and the activation gate. Finally, because simultaneous Ca^{2+} binding to the orthosteric sites hinders assessment of the third site's Ca^{2+} sensitivity, we generated the QA/EK/DR construct and used it to reliably measure the Ca^{2+} sensitivity of the third site. This approach allowed us to reveal that the

third Ca^{2+} site possesses a high affinity for Ca^{2+} with an apparent dissociation constant (K_D) of ~320 nM, which is well suited for sensing physiological Ca^{2+} concentrations (Figure 4B; Table S1). Our comprehensive mutagenesis experiments, in conjunction with double-mutant cycle analyses, further support that the three acidic residues E425, D879, and D884 directly participate in Ca^{2+} binding, whereas K428 serves a stabilizing structural role (Figures 4 and 5). Interestingly, in addition to impairing Ca^{2+} binding, disruption of the third Ca^{2+} site also differentially alters channel gating in a Ca^{2+}-independent manner (Figure 3; Figure S2), consistent with a pleiotropic role of these residues in both mediating Ca^{2+} binding and regulating the channel's gate.

Conformationally Restricting TM2–TM10 at the Third Site Inhibits Channel Activation

Our observation that chemically bridging E425C and D879C inhibits TMEM16A activation is both striking and counterintuitive, considering that Ca^{2+} binding to the third site promotes channel opening (Figure 4B). However, this is unsurprising, as we believe that Cd^{2+}-mediated metal bridging likely elicits distinct effects from Ca^{2+} binding to an intact third site based on the following reasons. First, in the intact site, the Ca^{2+} ion is coordinated by the acidic residues E425, D879, and D884 (Figures 4 and 5) (Alvadia et al., 2019; Bushell et al., 2019), while in the double cysteine-substituted mutant, Cd^{2+} should be sandwiched between E425C and D879C. Second, given the shorter side chain of cysteine compared with those of aspartate and glutamate, the conformation resulting from Cd^{2+}-E425C/D879C complex formation should, therefore, be distinct from that induced by Ca^{2+} binding to the intact site. Finally, Cd^{2+} coordination with E425C and D879C is more stable than Ca^{2+} within the third-site acidic residues, as signified by the extremely slow off-rate of Cd^{2+} that is characteristic of a cadmium-cysteine metal bridge (Figure 6) (Linsdell, 2015). Although precisely how such stabilization of TM2 and TM10 prohibits channel activation requires additional studies, our data further underscore the importance of this site in channel gating.

Potential Role of TM10' in Allosteric Modulation by the Third Ca^{2+} Site

Our functional evidence suggests that Ca^{2+} binding to the third site can lead to long-range allosteric effects on TMEM16A activation. However, it is still unclear how Ca^{2+} binding energy at the third site is propagated to the pore-gate domain. We speculate that TM10', a short α helix following TM10, may play an important role in mediating this allosteric coupling based on the following observations (Figure 7A). First, it was shown that replacing or truncating the C-terminal region following TM10' after the third Ca^{2+} site at L904 (Dang et al., 2017) or K895 (Scudieri et al., 2016) markedly altered the Ca^{2+} sensitivity of TMEM16A. Second, using chemical crosslinking experiments, Scudieri et al. (2016) suggested that TM10' may regulate channel gating via its inter-subunit coupling to the TM2–TM3 loop, which was previously implicated in TMEM16A's voltage-dependent channel activation (Ferrera et al., 2009; Xiao et al., 2011). Finally, the recent structural study of TMEM16K suggested that TM10' forms an inter-subunit contact with the TM2–TM3 loop (mostly β9–β10) and undergoes a pronounced swinging movement during Ca^{2+}-dependent activation; this enables rearrangement of the TM2–TM3 loop and, subsequently, the N-terminal cytosolic domain (NCD), all of which culminate in the opening of TMEM16K's lipid pathway (Bushell et al., 2019). On the basis of these structural and functional observations, we suggest that Ca^{2+} binding to the third site in TM2–TM10 likely

induces a conformational change of TM10', perhaps altering its inter-subunit interaction with the TM2–TM3 loop and, subsequently, the NCD to modulate channel opening (Figure 7A). The lack of conformational changes at the third site upon Ca^{2+} binding in the TMEM16A and TMEM16F structures likely reflects their desensitized/rundown states after Ca^{2+}-dependent activation (Alvadia et al., 2019; Bushell et al., 2019; Dang et al., 2017; Feng et al., 2019; Le et al., 2019a; Ye et al., 2018). Future studies are required to fully elaborate the molecular basis of this long-range allosteric coupling pathway between the third Ca^{2+} site and the activation gate (Figure 7B).

In summary, our work builds upon previous structural studies and provides the physical basis underlying a long-range regulatory gating mechanism by which Ca^{2+} binding to the TM2–TM10 site enhances channel opening. Our present findings also suggest that structurally conserved TMEM16 ion channels and scramblases may exploit a similar mode of allosteric regulation by Ca^{2+}. We believe that the additional Ca^{2+} site endows TMEM16 proteins with enhanced regulatory mechanisms, increasing their complexity necessary for diverse Ca^{2+} signaling functions in various tissues. Mechanistic insight into this Ca^{2+} binding site not only facilitates our understanding of the patho-physiology of TMEM16 mutations but may also assist future therapeutic design of allosteric modulators for the treatment of TMEM16-related diseases.

STAR★METHODS

RESOURCE AVAILABILITY

Lead Contact—Further information and requests for resources and reagents should be directed to and will be fulfilled by the Lead Contact, Huanghe Yang (huanghe.yang@duke.edu).

Materials Availability—This study did not generate new unique reagents.

Data and Code Availability—This study did not generate unique datasets/code.

EXPERIMENTAL MODEL AND SUBJECT DETAILS

Cell lines—Adherent human embryonic kidney 293T (HEK293T) cells, which were authenticated and tested negative for mycoplasma, were obtained from Duke Cell Culture Facility (ATCC CRL-11268). HEK293T cells were maintained in Dulbecco's Modified Eagle Medium (DMEM, GIBCO) supplemented with 10% fetal bovine serum (FBS, Sigma), 1% penicillin/streptomycin (GIBCO) in an incubator supplied with 5% CO_2 and kept at 37°C. HEK293T cells were passaged every 2–3 days and were used within 15 passages.

METHOD DETAILS

Cloning and Cell Culture—Mouse TMEM16A (mTMEM16A, NCBI accession code NP_001229278) tagged with a C-terminal EGFP (in an N1 vector) was used for all experiments. This mTMEM16A('a') isoform lacks the EAVK segment ('c') in the first intracellular loop. Individual point mutations of TMEM16A were generated using QuikChange site-directed mutagenesis kit (Agilent), and multiple mutations were generated

sequentially. All PCR primers were purchased from IDT DNA Technologies (see Table S2 the complete list of primers used for mutagenesis). Substituted amino acid sequences were validated by Sanger sequencing (Genewiz). Glass coverslips were pre-coated with poly-L-lysine (Sigma) and laminin (Sigma) for at least 1–2 h in a 24-well plate (Eppendorf) and were seeded with freshly dissociated HEK293T cells. HEK293T cells were transiently transfected in the following day using X-tremeGENE 9 DNA transfection reagent (Sigma). Each well was typically transfected with 200 to 250 ng of total DNA plasmid to achieve sufficient expression for current recordings.

Electrophysiology—Electrophysiology recordings were performed at room temperature within 24 to 36 h after transfection. Glass electrodes were made by pulling borosilicate capillaries (Sutter Instruments) and fire-polished with a microforge (Narishige). Electrodes typically had a resistance of 2–3 MΩ when filled with recording solutions. Excised inside-out membrane patches were obtained by rapidly pulling gigaohm (GΩ) cell-attached seals from HEK293T cells expressing fluorescently tagged TMEM16A channels.

External (pipette) solution contains 140 mM NaCl, 10 mM HEPES, 2 mM $MgCl_2$, and pH 7.3 (adjusted with NaOH). Bath solution contains 140 mM NaCl, 10 mM HEPES, 5 mM EGTA, and pH 7.4 (adjusted with NaOH). Intracellular (perfusion) solutions with less than 100 μM Ca^{2+} contain were made by adding $CaCl_2$ to a solution containing 140 mM NaCl, 10 mM HEPES, 5 mM EGTA, and the amount of $CaCl_2$ added was calculated using WEBMAXC (https://somapp.ucdmc.ucdavis.edu/pharmacology/bers/maxchelator/) to achieve desired free Ca^{2+}. The free Ca^{2+} concentrations were further corrected using the ratiometric Ca^{2+} dye Fura-2 (ATT Bioquest) by fitting their absorbances against a standard Ca^{2+} curve generated from a Ca^{2+} calibration kit (Biotum). For solution with 100 μM or 500 μM Ca^{2+}, $CaCl_2$ was directly added to a solution containing 140 mM NaCl, 10 mM HEPES, pH 7.3.

Application of intracellular solutions to excised inside-out patches was carried out using a pressurized perfusion apparatus (ALA-VM8, ALA Scientific Instruments) in which the glass electrodes containing the excised patches were placed directly in front of the perfusion outlet. For measurements of the Ca^{2+}-dependent dose-response behavior of TMEM16A WT and mutant channels with intact (WT or Q645A backgrounds) or disrupted (QA/EK/DR background) orthosteric Ca^{2+} sites, excised inside-out patches were held at +60 mV and TMEM16A-mediated outward currents (Cl^- influx) were elicited by sequential application of EGTA-buffered internal solutions containing increasing Ca^{2+} concentrations. Once the Ca^{2+}-elicited currents reached a steady state, a Ca^{2+}-free solution (140 mM NaCl, 10 mM HEPES, 5 mM EGTA, pH 7.3) was immediately applied to allow the channels to return the closed state (WT background channels) or the basal activity level (QA/EK/DR background channels). To ensure that current rundown does not impact our Ca^{2+}-dependent measurements and quantifications, we also performed Ca^{2+}-dependent recordings of the QA/EK/DR mutant using a rundown-corrected protocol akin to one reported previously (Lim et al., 2016; Ni et al., 2014). In this rundown-corrected protocol, after application of each test Ca^{2+} concentration (0.255, 0.387, 0.94, 2.26, 6 and 100 μM), saturating 500 μM Ca^{2+} was applied to obtain the reference peak current, which was used for normalizing the test Ca^{2+} current responses.

For current-voltage (*I-V*) recordings of the Q645A background construct-containing TMEM16A mutant channels in the absence of Ca^{2+}, the excised membrane patches were held at 60 mV, and test voltage steps from 120 to +140 mV were applied to elicit channel opening in the absence of 0 Ca^{2+}. The same patch was immediately exposed to 100 μM Ca^{2+} and subjected to an *I-V* protocol in which the membrane was held at 0 mV and stepped to +140 mV and 60 mV. The steady-state currents measured during test voltage steps were used for subsequent analysis.

For cadmium (Cd^{2+}) metal bridging experiments, the desired Cd^{2+} concentrations were directly added to a solution containing 140 mM NaCl, 10 mM HEPES, 100 μM Ca^{2+}, pH 7.4 using 1000× Cd^{2+} stock solutions. 1000× Cd^{2+} stock solutions (0.5, 1, 10 mM) were made from 10× serial dilutions from a 100 mM Cd^{2+} stock solution using ultrapure water (Invitrogen). Excised inside-out patches were held at +60 mV using a gap-free protocol and TMEM16A channels were activated with the control 100 μM or 500 μM Ca^{2+} solution for 2–3 s to obtain the reference peak current before being switched to a Cd^{2+}-containing solution to assess current inhibition. Application of Cd^{2+}-containing solution usually took 4–5 s until the appearance of the steady-state currents after which the control 100 μM or 500 μM Ca^{2+} solution was re-applied (for ~30 s) to allow current recovery from Cd^{2+}-mediated inhibition.

For experiments assessing the effects of Cd^{2+} metal bridge formation in the absence of Ca^{2+}, E425C/D879C(QA/EK/DR) and E425C/D879C(QA/EK/DR) channels were first activated in the absence of Ca^{2+} and immediately exposed to solution containing 10 μM Cd^{2+} (140 mM NaCl, 10 HEPES, pH 7.4) using an *I-V* protocol. The membrane was held at 60 mV and the channels were activated via voltage steps from 120 to +140 mV. The E425C/D884C(QA/EK/DR) was used as a negative control for its lack of Cd^{2+} sensitivity as seen in the WT background (see Figures S6B, S6D, and S6E).

All electrophysiology recordings were low-pass filtered at 5 kHz (Axopatch 200B) and digitally sampled at 10 kHz (Axon Digidata 1550A) and digitized by Clampex 10 (Molecular Devices).

Confocal microscopy—HEK293T cells were co-transfected with EGFP-tagged mouse TMEM16A mutant channels (mTMEM16A-EGFP) and OFPSpark®-tagged human phospholipid scramblase 1 (hPLSCR1-OFPSpark®, Sino Biological) at a 2:1 DNA ratio. hPLSCR1 is a single-pass transmembrane protein that favors plasma membrane expression (Sun et al., 2002). The fluorescently tagged hPLSCR1 was used as a plasma membrane marker in this study. Cells were imaged approximately 24–30 h after transfection. Fluorescent images were acquired using a Zeiss 780 inverted confocal microscope at 60x magnification.

QUANTIFICATION AND STATISTICAL ANALYSIS

Electrophysiological data analysis was done in Clampfit, Microsoft Excel and MATLAB (MathWorks). Fluorescence image analysis was done in ImageJ (https://imagej.nih.gov/ij/).

Ca^{2+}-dependent channel activation—For WT and mutant channels with intact orthosteric Ca^{2+} sites, the Ca^{2+}-elicited steady-state currents were normalized to the peak current (see Figure 2). For TMEM16A mutant channels with impaired orthosteric Ca^{2+} sites (QA/EK/DR containing constructs), the basal current right after each Ca^{2+} application was subtracted from the steady-state Ca^{2+}-elicited current to avoid the issue with changing basal current, and these Ca^{2+}-sensitive current components (see Figures 4B, 4G, and 5E) were then normalized to the peak Ca^{2+}-sensitive current (see Figures 4H, 5G, and 5I). For rundown-corrected Ca^{2+}-dependent measurements of the QA/EK/DR mutant (Figures S3A–S3C), the Ca^{2+}-sensitive current of each test Ca^{2+} concentration was normalized to its respective reference peak current elicited by 500 μM Ca^{2+}, and these reference peak-normalized values of the test Ca^{2+} concentrations were used for constructing the dose-response curves. In all cases, the sigmoidal Ca^{2+} dose-response curves were similarly constructed by fitting the normalized Ca^{2+}-elicited currents using a non-linear regression curve fit with the equation:

$$\frac{1}{I_{max}} = \frac{1}{1 + \left(\frac{[EC_{50}]}{[Ca^{2+}]}\right)^{H}} \quad \text{(Equation 1)}$$

where I/I_{max} is the normalized Ca^{2+}-elicited current, $[Ca^{2+}]$ is the applied free Ca^{2+} concentration, H is the Hill coefficient, and EC_{50} is the estimated concentration of Ca^{2+} at which I/I_{max} is 0.5. The EC_{50} values from individual recordings are extracted for statistical analyses.

Cd^{2+} metal bridging experiments—The extent of Cd^{2+}-mediated inhibition of TMEM16A in the presence of 100 μM Ca^{2+} was determined as:

$$Current\,ratio(\%) = \frac{I_{Cd^{2+}}}{I_{peak}} \times 100 \quad \text{(Equation 2)}$$

where I_{peak} and I_{Cd2+} denote steady-state currents measured in the presence of 100 μM or 500 μM Ca^{2+} before and during Cd^{2+} application, respectively.

To assess the extent of current recovery following Cd^{2+} treatment, we determined the apparent off-rate of Cd^{2+} (Figure 6F; Figure S6E). As in the case of Cd^{2+}-insensitive channels such as WT or the single cysteine mutants E425C, D879C, the rapid current recovery of inhibition following Cd^{2+} washout mostly represents the rate of displacement of Cd^{2+} from the orthosteric Ca^{2+} binding sites (Figures 6A and 6E; Figure S5). On the other hand, in the Cd^{2+}-sensitive double mutant E425C/D879C, the tight association between Cd^{2+} and the substituted cysteines E425C and D879C mostly accounts for the much slower recovery rate (Figures 6B and 6E; Figure S5). As a result, we used the time constant (τ) of current recovery after application of 1 μM Cd^{2+} to quantitatively assess the effects of Cd^{2+} crosslinking by fitting the recovering current with a standard exponential fit with the equation:

$$I_{(t)} = I_0 + A\left(1 - e^{\frac{-t}{\tau}}\right) \quad \text{(Equation 3)}$$

where $I_{(t)}$ represents the current at time point t, I_0 is the initial current amplitude, t is the time constant.

Current-voltage (I-V) recordings—For *I-V* measurements of Q645A mutant channels, we used the steady state currents obtained during the depolarization steps for analysis due to the rapid deactivation at hyperpolarization and the intrinsically low open probability of the Q645A mutant in the absence of Ca^{2+} binding to the orthosteric sites (Lam and Dutzler, 2018; Peters et al., 2018). The calculated conductance from each test voltage step measured in the absence of Ca^{2+} (first recording) was normalized to the peak conductance measured at +140 mV in the presence of 100 μM Ca^{2+} (second recording). The resulting normalized G/G_{max}-V curves were fit with a Boltzmann equation:

$$\frac{G}{G_{max}} = \frac{1}{1 + e^{\frac{-zF(Vm - V_{1/2})}{RT}}} \quad \text{(Equation 4)}$$

where G/G_{max} is the normalized channel conductance, z is the number of equivalent gating charges, V_m is the applied membrane voltage, $V_{1/2}$ is the estimated voltage at which G/G_{max} is 0.5, F is the Faraday's constant, R is the gas constant, and T is the absolute temperature. Because of the low open probability of the Q645A-containing mutants in 0 Ca^{2+}, their G/G_{max}-V curves did not go beyond 0.5 (Figure 3F). We therefore did not extract the $V_{1/2}$ values for further comparisons.

Double mutant cycle analysis—To assess the potential energetic coupling between the charged residues at the third Ca^{2+} site, we extracted the Ca^{2+} EC_{50} values from our Ca^{2+}-dependent dose-response measurements of single and double mutations of the third Ca^{2+} site in the QA/EK/DR background. Because we were able to reliably measure the Ca^{2+} dose-response curves of K428A/D879A(QA/EK/DR) and K428A/D884A(QA/EK/DR), the K428-D879 and K428-D884 residue pairs were further analyzed using double mutant cycle analysis by calculating the free energy change associated with a perturbation (Hidalgo and MacKinnon, 1995). For each pair of residues, namely X and Y, the free energy change associated with their perturbations via single or double mutations was calculated using the following equations:

$$\Delta G_{XY > X'Y} = RT * In\left(\frac{EC_{50(X'Y))}}{EC_{50(XY)}}\right)\left(\text{or } \Delta G_{(1)}\right) \quad \text{(Equation 5)}$$

$$\Delta G_{XY' > X'Y'} = RT * In\left(\frac{EC_{50(X'Y')}}{EC_{50(XY')}}\right)\left(\text{or } \Delta G_{(4)}\right) \quad \text{(Equation 6)}$$

$$\Delta G_{XY > XY'} = RT * In\left(\frac{EC_{50(XY')}}{EC_{50(XY)}}\right)\left(\text{or } \Delta G_{(2)}\right) \quad \text{(Equation 7)}$$

$$\Delta G_{X'Y > X'Y'} = RT * In\left(\frac{EC_{50(X'Y')}}{EC_{50(X'Y)}}\right)\left(\text{or } \Delta G_{(3)}\right) \quad \text{(Equation 8)}$$

where XY denotes intact residues on the background; X'Y, XY', X'Y' denote mutations at X, Y, and both, respectively; EC_{50} is the estimated half-maximal activation concentration of Ca^{2+}. Note that the background refers the QA/EK/DR construct on which single and double mutations of the third site residue pairs are made. In principle, $\Delta G_{(1)}$ and $\Delta G_{(4)}$ are related and represent the free energy change as a result of mutation of X (or X') on the background channel ($\Delta G_{(1)}$) or on the Y' background ($\Delta G_{(4)}$). Similarly, $\Delta G_{(2)}$ and $\Delta G_{(3)}$ represent the free change associated with Y' mutations on background and X' background, respectively. If X and Y residues are energetically coupled, the free energy change associated with the double mutations–X' mutation on Y' background ($\Delta G_{(4)}$) or Y' mutation on X' background ($\Delta G_{(3)}$)–would differ from that associated with the single mutations X' and Y', or $\Delta G_{(1)}$ and $\Delta G_{(2)}$, respectively. Please also refer to Figures 5G–5J for the schematic diagrams of our double mutant cycle analyses. To obtain the standard error for the interaction energy ($\Delta\Delta G_{int}$), the individually calculated free energy change ($\Delta G_{(s)}$) values were used as:

$$\Delta\Delta G_{int} = \Delta G_{(4)} - \Delta G_{(1)} = \Delta G_{(3)} - \Delta G_{(2)} \quad \text{(Equation 9)}$$

The calculated $\Delta\Delta G_{int}$ values were subsequently confirmed using the equation:

$$\Delta\Delta G_{int} = RT * In\left(\frac{EC_{50(X'Y')} \cdot EC_{50(bg)}}{EC_{50(X'Y)} \cdot EC_{50(XY')}}\right) \quad \text{(Equation 10)}$$

Structural and sequence analysis—PDB coordinate files were obtained from the Protein Data Bank (https://www.rcsb.org/). Protein structure figures were prepared in Pymol (Schrödinger, Inc.). Protein sequence alignment was done in UniProt (https://www.uniprot.org/align/).

Statistical analysis—Statistical analyses were performed in Prism software (GraphPad). Two-tailed Student's t test was used for comparisons between two groups (paired or unpaired), and one-way ANOVA was used for comparisons between multiple data groups. Comparisons with p values < 0.05 are deemed to be statistically significant. Data in summary bar graphs are represented as mean ± standard deviation (SD) or mean ± standard error of the mean (s.e.m.), and each data point represents an independent recording. *, **, *** and **** represent statistical significance corresponding to p value < 0.05, < 0.01, < 0.001, < 0.0001, respectively.

Supplementary Material

Refer to Web version on PubMed Central for supplementary material.

ACKNOWLEDGMENTS

We thank Dr. Yang Zhang for help with confocal microscopy, Dr. Terrance G. Oas for help with double-mutant cycle analysis, and Atul K. Rangadurai and Michael Young for their critical comments on the manuscript. This work was supported by NIH grant DP2-GM126898 (to H.Y.) and American Heart Association Pre-Doctoral fellowship 19PRE34380456 (to S.C.L.).

REFERENCES

Alvadia C, Lim NK, Clerico Mosina V, Oostergetel GT, Dutzler R, and Paulino C (2019). Cryo-EM structures and functional characterization of the murine lipid scramblase TMEM16F. eLife 8, e44365. [PubMed: 30785399]

Balreira A, Boczonadi V, Barca E, Pyle A, Bansagi B, Appleton M, Graham C, Hargreaves IP, Rasic VM, Lochmüller H, et al. (2014). ANO10 mutations cause ataxia and coenzyme Q_{10} deficiency. J. Neurol 261, 2192–2198. [PubMed: 25182700]

Brunner JD, Lim NK, Schenck S, Duerst A, and Dutzler R (2014). X-ray structure of a calcium-activated TMEM16 lipid scramblase. Nature 516, 207–212. [PubMed: 25383531]

Bushell SR, Pike ACW, Falzone ME, Rorsman NJG, Ta CM, Corey RA, Newport TD, Christianson JC, Scofano LF, Shintre CA, et al. (2019). The structural basis of lipid scrambling and inactivation in the endoplasmic reticulum scramblase TMEM16K. Nat. Commun 10, 3956. [PubMed: 31477691]

Caputo A, Caci E, Ferrera L, Pedemonte N, Barsanti C, Sondo E, Pfeffer U, Ravazzolo R, Zegarra-Moran O, and Galietta LJ (2008). TMEM16A, a membrane protein associated with calcium-dependent chloride channel activity. Science 322, 590–594. [PubMed: 18772398]

Changeux JP, and Christopoulos A (2016). Allosteric Modulation as a Unifying Mechanism for Receptor Function and Regulation. Cell 166, 1084–1102. [PubMed: 27565340]

Cho CH, Lee S, Kim A, Yarishkin O, Ryoo K, Lee YS, Jung HG, Yang E, Lee DY, Lee B, et al. (2020). TMEM16A expression in cholinergic neurons of the medial habenula mediates anxiety-related behaviors. EMBO Rep. 21, e48097. [PubMed: 31782602]

Crottès D, and Jan LY (2019). The multifaceted role of TMEM16A in cancer. Cell Calcium 82, 102050. [PubMed: 31279157]

Dang S, Feng S, Tien J, Peters CJ, Bulkley D, Lolicato M, Zhao J, Zuberbühler K, Ye W, Qi L, et al. (2017). Cryo-EM structures of the TMEM16A calcium-activated chloride channel. Nature 552, 426–429. [PubMed: 29236684]

De Jesús-Pérez JJ, Cruz-Rangel S, Espino-Saldaña AE, Martínez-Torres A, Qu Z, Hartzell HC, Corral-Fernandez NE, Pérez-Cornejo P, and Arreola J (2018). Phosphatidylinositol 4,5-bisphosphate, cholesterol, and fatty acids modulate the calcium-activated chloride channel TMEM16A (ANO1). Biochim. Biophys. Acta Mol. Cell Biol. Lipids 1863, 299–312. [PubMed: 29277655]

Falzone ME, Malvezzi M, Lee BC, and Accardi A (2018). Known structures and unknown mechanisms of TMEM16 scramblases and channels. J. Gen. Physiol 150, 933–947. [PubMed: 29915161]

Feng S, Dang S, Han TW, Ye W, Jin P, Cheng T, Li J, Jan YN, Jan LY, and Cheng Y (2019). Cryo-EM Studies of TMEM16F Calcium-Activated Ion Channel Suggest Features Important for Lipid Scrambling. Cell Rep. 28, 567–579.e4. [PubMed: 31291589]

Ferrera L, Caputo A, Ubby I, Bussani E, Zegarra-Moran O, Ravazzolo R, Pagani F, and Galietta LJ (2009). Regulation of TMEM16A chloride channel properties by alternative splicing. J. Biol. Chem 284, 33360–33368. [PubMed: 19819874]

Hidalgo P, and MacKinnon R (1995). Revealing the architecture of a K+ channel pore through mutant cycles with a peptide inhibitor. Science 268, 307–310. [PubMed: 7716527]

Hite RK, Tao X, and MacKinnon R (2017). Structural basis for gating the high-conductance Ca^{2+}-activated K^{+} channel. Nature 541, 52–57. [PubMed: 27974801]

Horrigan FT (2012). Perspectives on: conformational coupling in ion channels: conformational coupling in BK potassium channels. J. Gen. Physiol 140, 625–634. [PubMed: 23183698]

Horrigan FT, and Aldrich RW (2002). Coupling between voltage sensor activation, Ca2+ binding and channel opening in large conductance (BK) potassium channels. J. Gen. Physiol 120, 267–305. [PubMed: 12198087]

Jeng G, Aggarwal M, Yu WP, and Chen TY (2016). Independent activation of distinct pores in dimeric TMEM16A channels. J. Gen. Physiol 148, 393–404. [PubMed: 27799319]

Lam AK, and Dutzler R (2018). Calcium-dependent electrostatic control of anion access to the pore of the calcium-activated chloride channel TMEM16A. eLife 7, e39122. [PubMed: 30311910]

Le SC, Jia Z, Chen J, and Yang H (2019a). Molecular basis of PIP_2-dependent regulation of the Ca^{2+}-activated chloride channel TMEM16A. Nat. Commun 10, 3769. [PubMed: 31434906]

Le T, Le SC, and Yang H (2019b). Drosophila Subdued is a moonlighting transmembrane protein 16 (TMEM16) that transports ions and phospholipids. J. Biol. Chem 294, 4529–4537. [PubMed: 30700552]

Lim NK, Lam AK, and Dutzler R (2016). Independent activation of ion conduction pores in the double-barreled calcium-activated chloride channel TMEM16A. J. Gen. Physiol 148, 375–392. [PubMed: 27799318]

Linsdell P (2015). Metal bridges to probe membrane ion channel structure and function. Biomol. Concepts 6, 191–203. [PubMed: 26103632]

Malvezzi M, Chalat M, Janjusevic R, Picollo A, Terashima H, Menon AK, and Accardi A (2013). Ca2+-dependent phospholipid scrambling by a reconstituted TMEM16 ion channel. Nat. Commun 4, 2367. [PubMed: 23996062]

Ni YL, Kuan AS, and Chen TY (2014). Activation and inhibition of TMEM16A calcium-activated chloride channels. PLoS ONE 9, e86734. [PubMed: 24489780]

Paulino C, Kalienkova V, Lam AKM, Neldner Y, and Dutzler R (2017a). Activation mechanism of the calcium-activated chloride channel TMEM16A revealed by cryo-EM. Nature 552, 421–425. [PubMed: 29236691]

Paulino C, Neldner Y, Lam AK, Kalienkova V, Brunner JD, Schenck S, and Dutzler R (2017b). Structural basis for anion conduction in the calcium-activated chloride channel TMEM16A. eLife 6, e26232. [PubMed: 28561733]

Peters CJ, Yu H, Tien J, Jan YN, Li M, and Jan LY (2015). Four basic residues critical for the ion selectivity and pore blocker sensitivity of TMEM16A calcium-activated chloride channels. Proc. Natl. Acad. Sci. USA 112, 3547–3552. [PubMed: 25733897]

Peters CJ, Gilchrist JM, Tien J, Bethel NP, Qi L, Chen T, Wang L, Jan YN, Grabe M, and Jan LY (2018). The Sixth Transmembrane Segment Is a Major Gating Component of the TMEM16A Calcium-Activated Chloride Channel. Neuron 97, 1063–1077.e4. [PubMed: 29478917]

Schroeder BC, Cheng T, Jan YN, and Jan LY (2008). Expression cloning of TMEM16A as a calcium-activated chloride channel subunit. Cell 134, 1019–1029. [PubMed: 18805094]

Scudieri P, Sondo E, Ferrera L, and Galietta LJ (2012). The anoctamin family: TMEM16A and TMEM16B as calcium-activated chloride channels. Exp. Physiol 97, 177–183. [PubMed: 21984732]

Scudieri P, Musante I, Gianotti A, Moran O, and Galietta LJ (2016). Inter-molecular Interactions in the TMEM16A Dimer Controlling Channel Activity. Sci. Rep 6, 38788. [PubMed: 27929144]

Sun J, Nanjundan M, Pike LJ, Wiedmer T, and Sims PJ (2002). Plasma membrane phospholipid scramblase 1 is enriched in lipid rafts and interacts with the epidermal growth factor receptor. Biochemistry 41, 6338–6345. [PubMed: 12009895]

Suzuki J, Umeda M, Sims PJ, and Nagata S (2010). Calcium-dependent phospholipid scrambling by TMEM16F. Nature 468, 834–838. [PubMed: 21107324]

Suzuki J, Fujii T, Imao T, Ishihara K, Kuba H, and Nagata S (2013). Calcium-dependent phospholipid scramblase activity of TMEM16 protein family members. J. Biol. Chem 288, 13305–13316. [PubMed: 23532839]

Ta CM, Acheson KE, Rorsman NJG, Jongkind RC, and Tammaro P (2017). Contrasting effects of phosphatidylinositol 4,5-bisphosphate on cloned TMEM16A and TMEM16B channels. Br. J. Pharmacol 174, 2984–2999. [PubMed: 28616863]

Tao X, Hite RK, and MacKinnon R (2017). Cryo-EM structure of the open high-conductance Ca2+-activated K+ channel. Nature 541, 46–51. [PubMed: 27974795]

Tembo M, Wozniak KL, Bainbridge RE, and Carlson AE (2019). Phosphatidylinositol 4,5-bisphosphate (PIP_2) and Ca^{2+} are both required to open the Cl^- channel TMEM16A. J. Biol. Chem 294, 12556–12564. [PubMed: 31266809]

Tien J, Peters CJ, Wong XM, Cheng T, Jan YN, Jan LY, and Yang H (2014). A comprehensive search for calcium binding sites critical for TMEM16A calcium-activated chloride channel activity. eLife 3, e02772.

Whitlock JM, and Hartzell HC (2017). Anoctamins/TMEM16 Proteins: Chloride Channels Flirting with Lipids and Extracellular Vesicles. Annu. Rev. Physiol 79, 119–143. [PubMed: 27860832]

Xiao Q, Yu K, Perez-Cornejo P, Cui Y, Arreola J, and Hartzell HC (2011). Voltage- and calcium-dependent gating of TMEM16A/Ano1 chloride channels are physically coupled by the first intracellular loop. Proc. Natl. Acad. Sci. USA 108, 8891–8896. [PubMed: 21555582]

Yang YD, Cho H, Koo JY, Tak MH, Cho Y, Shim WS, Park SP, Lee J, Lee B, Kim BM, et al. (2008). TMEM16A confers receptor-activated calcium-dependent chloride conductance. Nature 455, 1210–1215. [PubMed: 18724360]

Yang H, Kim A, David T, Palmer D, Jin T, Tien J, Huang F, Cheng T, Coughlin SR, Jan YN, and Jan LY (2012). TMEM16F forms a Ca2+-activated cation channel required for lipid scrambling in platelets during blood coagulation. Cell 151, 111–122. [PubMed: 23021219]

Yang H, Zhang G, and Cui J (2015). BK channels: multiple sensors, one activation gate. Front. Physiol 6, 29. [PubMed: 25705194]

Ye W, Han TW, Nassar LM, Zubia M, Jan YN, and Jan LY (2018). Phosphatidylinositol-(4, 5)-bisphosphate regulates calcium gating of small-conductance cation channel TMEM16F. Proc. Natl. Acad. Sci. USA 115, E1667–E1674. [PubMed: 29382763]

Yu K, Duran C, Qu Z, Cui YY, and Hartzell HC (2012). Explaining calcium-dependent gating of anoctamin-1 chloride channels requires a revised topology. Circ. Res 110, 990–999. [PubMed: 22394518]

Yu K, Jiang T, Cui Y, Tajkhorshid E, and Hartzell HC (2019). A network of phosphatidylinositol 4,5-bisphosphate binding sites regulates gating of the Ca2+-activated Cl− channel ANO1 (TMEM16A). Proc. Natl. Acad. Sci. USA 116, 19952–19962. [PubMed: 31515451]

Zhou Y, Yang H, Cui J, and Lingle CJ (2017). Threading the biophysics of mammalian Slo1 channels onto structures of an invertebrate Slo1 channel. J. Gen. Physiol 149, 985–1007. [PubMed: 29025867]

Highlights

- TMEM16A possesses a third high-affinity Ca^{2+} binding site between TM2 and TM10
- Binding of Ca^{2+} to the third Ca^{2+} site allosterically promotes channel opening
- Neutralizing coordinating residues abolishes Ca^{2+} binding to the third site
- An engineered Cd^{2+} metal bridge at the third Ca^{2+} site inhibits channel activation

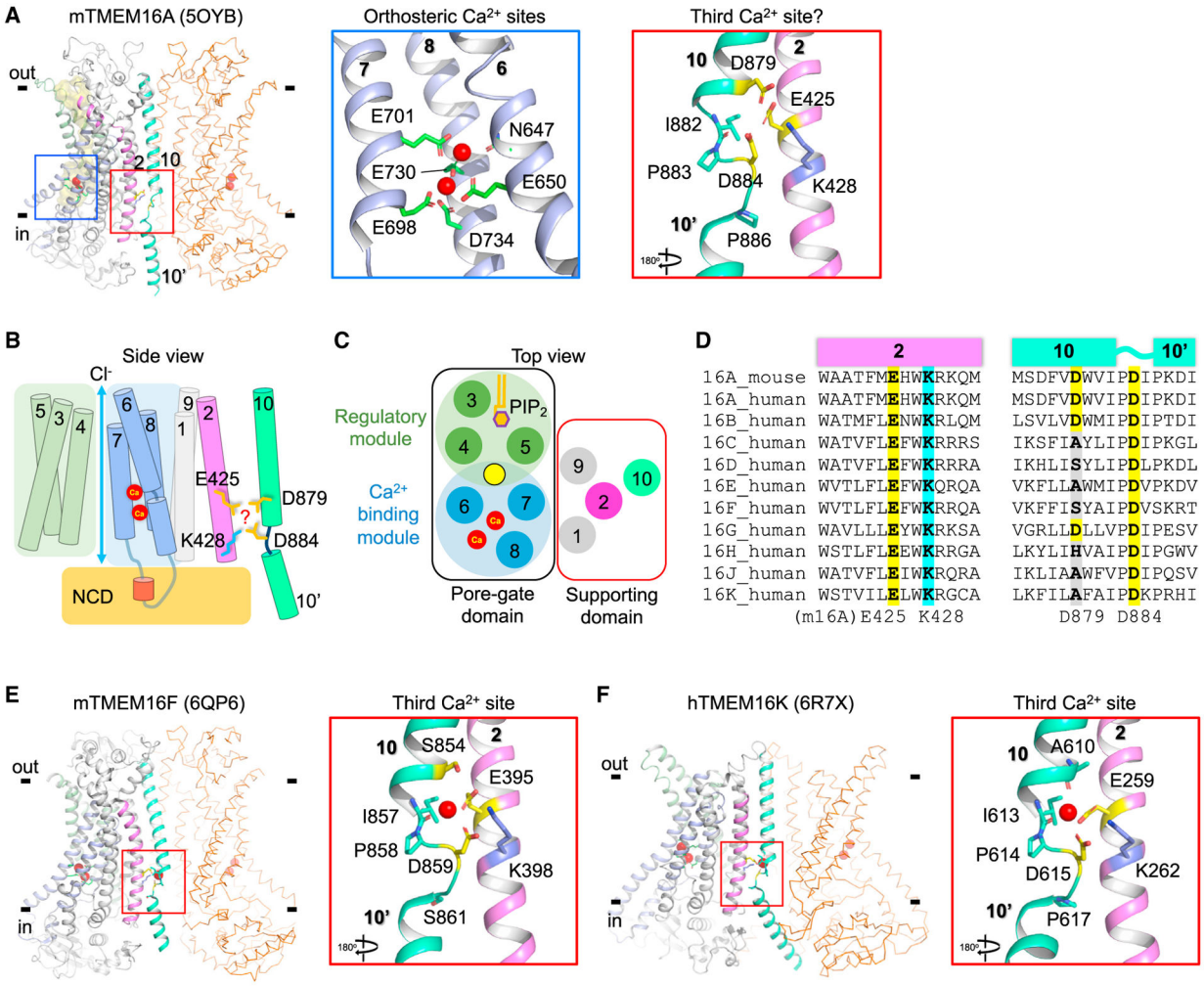

Figure 1. An Additional Ca^{2+} Binding Site in TMEM16 Ion Channels and Scramblases

(A) Structure of the Ca^{2+}-bound mouse TMEM16A homodimer (PDB: 5OYB). The anion permeation pathway in one monomer is shown as a yellow surface. TMs 2 and 10 are indicated in magenta and cyan, respectively; TMs 6, 7, and 8 are indicated in light blue; and Ca^{2+} ions are indicated as red spheres. The second monomer is indicated as orange ribbons. Insets, close-up views of the orthosteric Ca^{2+} binding sites (blue box) and the putative third Ca^{2+} site (red box). Out: extracellular; in: intracellular.

(B and C) Cartoon representation of TMEM16A showing the proposed modular design as viewed from the side (B) or top (C) (Le et al., 2019a).

(D) Protein sequence alignment of TMEM16 proteins at the third Ca^{2+} binding site in TM2 and TM10.

(E and F) The Ca^{2+}-bound structures of mouse TMEM16F (PDB: 6QP6) (E) and human TMEM16K (PDB: 6R7X) (F). Insets indicate their respective third Ca^{2+} sites in TM2 and TM10.

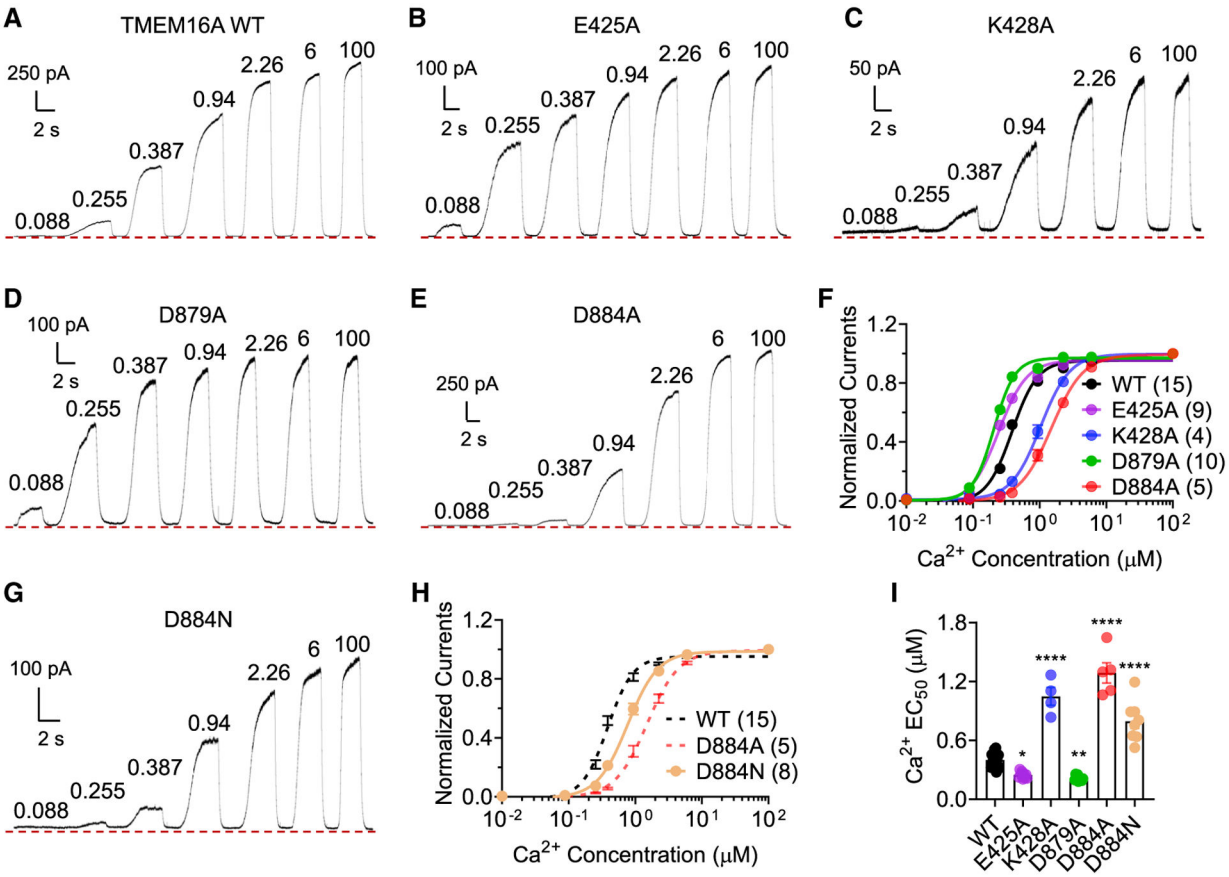

Figure 2. Mutations at the Putative Third Ca^{2+} Site Alter TMEM16A's Ca^{2+} Sensitivity

(A–E) Representative recordings showing Ca^{2+}-dependent activation of TMEM16A wild type (WT) (A), E425A (B), K428A (C), D879A (D), and D884A (E). Ca^{2+} concentrations are shown as numbers above outward current deflections (in micromolar). The membrane was held at +60 mV. Red dashed line indicates 0-pA baseline.

(F) The Ca^{2+} dose-response curves of TMEM16A WT and mutants.

(G and H) Representative recording showing Ca^{2+}-dependent activation of TMEM16A D884N (G) and its dose-response curve (H).

(I) Quantifications of the half-maximal activation concentration of Ca^{2+} (Ca^{2+} EC_{50}) values of TMEM16A WT and mutants (see also Table S1).

Numbers in parentheses denote the number of individual recordings. One-way ANOVA: p values are 0.0244, <0.0001, 0.0027, <0.0001, and <0.0001 for E425A, K428A, D879A, D884A, and D884N, respectively. Data are represented as means ± SEM.

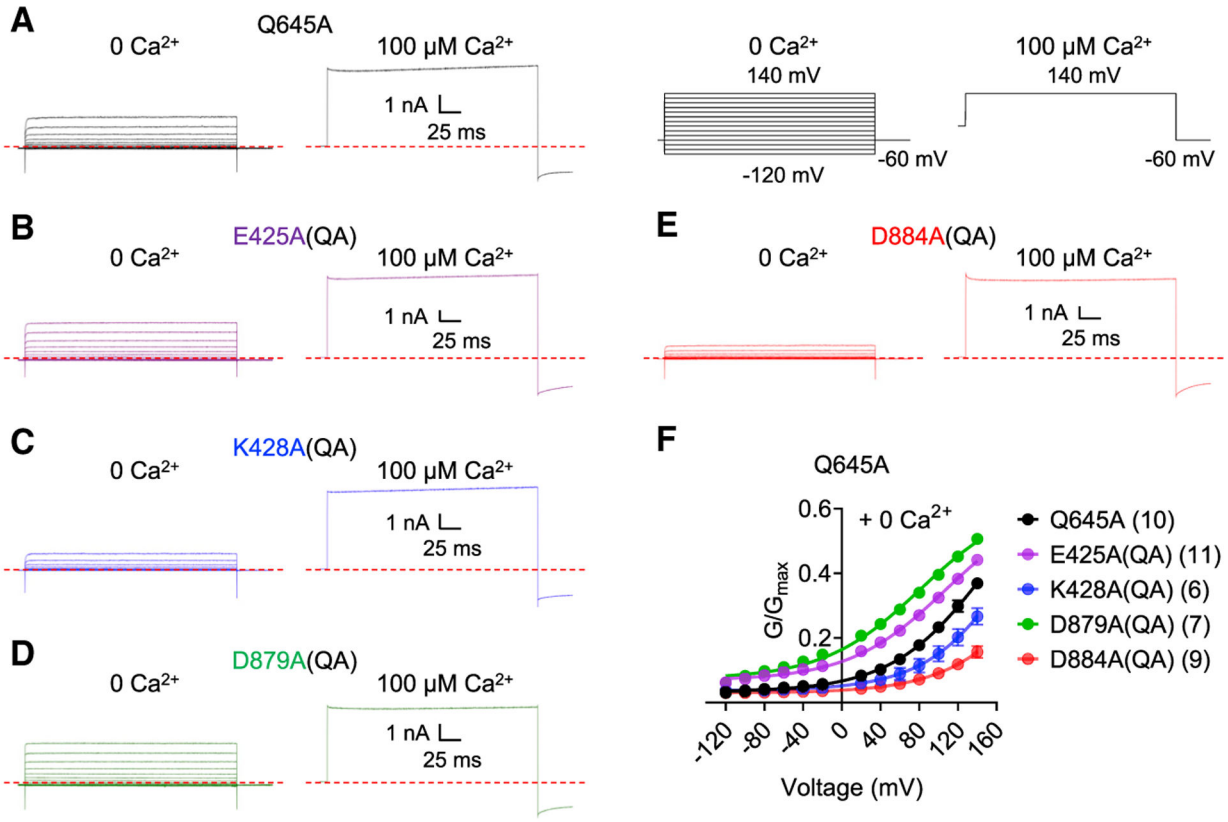

Figure 3. Mutation of the Third Ca^{2+} Site Residues Directly Affects Channel Gating independent of Ca^{2+}

(A–E) Representative voltage-current (I-V) measurements of TMEM16A Q645A (A, or QA background construct), E425A(QA) (B), K428A(QA) (C), D879A(QA) (D), and D884A(QA) (E) The same membrane patch was sequentially recorded in 0 μM Ca^{2+} (left recording) and then in 100 μM Ca^{2+} to obtain maximum current (right recording). Voltage protocols are indicated in (A) (right).

(F) Ca^{2+}-independent conductance-voltage (G-V) curves of QA mutants. Numbers in parentheses denote the number of individual recordings. Data are represented as mean ± SEM.

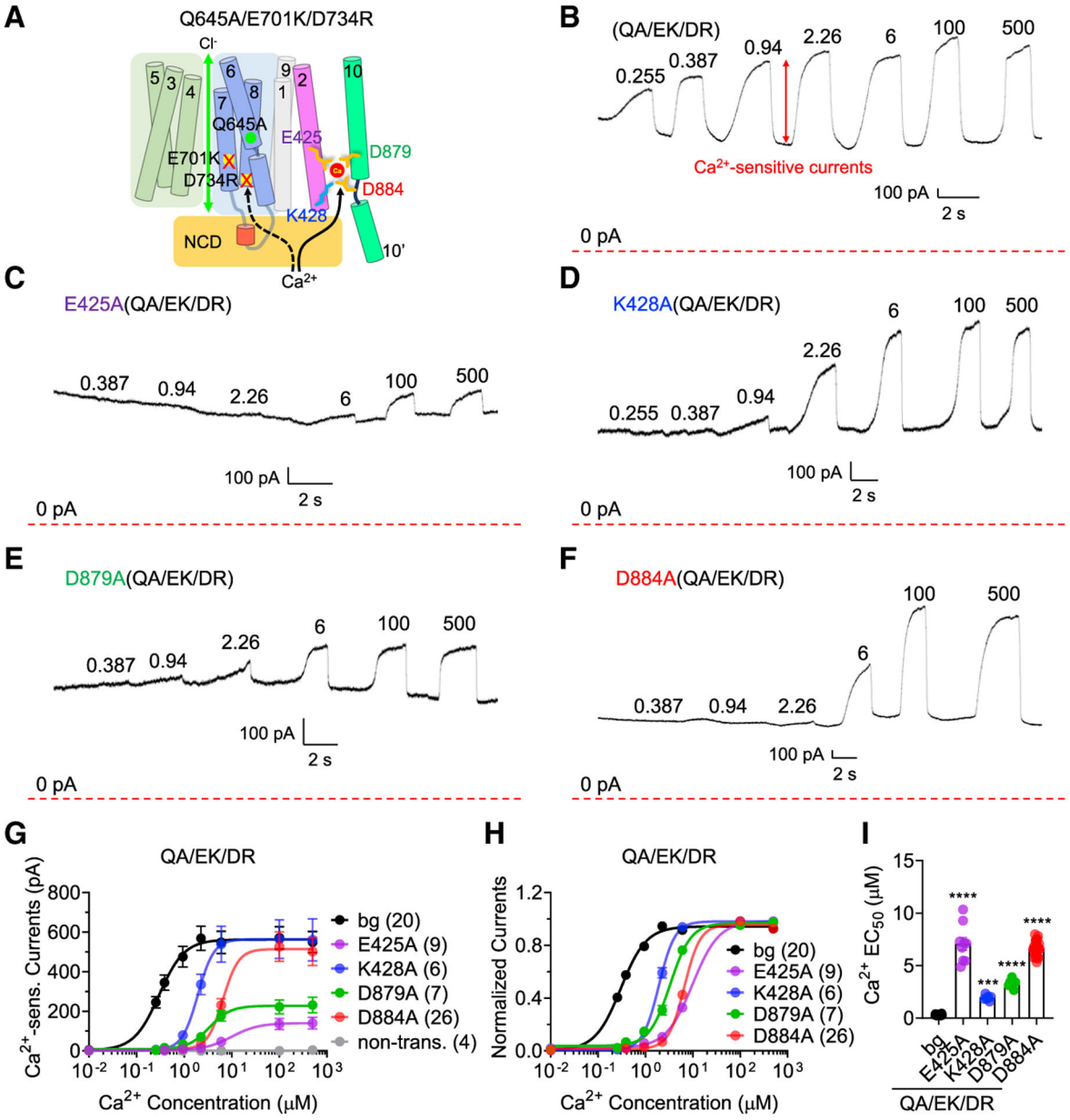

Figure 4. Single Alanine Mutations of the Third Ca^{2+} Site Residues Reduce Ca^{2+} Binding

(A) Schematic diagram showing the experimental design. E701K and D734R mutations were introduced to the Q645A background to abolish Ca^{2+} binding to the orthosteric sites. The Q645A mutation enables channel activation in absence of Ca^{2+} binding to the orthosteric sites.

(B–F) Representative Ca^{2+}-activated currents of the Q645A/E701K/D734R background (B, QA/EK/DR), or QA/EK/DR carrying an additional alanine mutation: E425A (C), K428A (D), D879A (E), and D884A (F). Ca^{2+} concentrations are shown as numbers above outward current deflections (in micromolar). The membrane was held at +60 mV. Red dashed line indicates 0-pA baseline.

(G) Quantifications of the Ca^{2+}-activated currents of TMEM16A mutants in response to different Ca^{2+} concentrations. bg, QA/EK/DR background; non-trans., non-transfected. (H and I) Normalized Ca^{2+} dose-response curves of QA/EK/DR background, K428A(QA/EK/DR), D879A (QA/EK/DR), and D884A(QA/EK/DR) (H) and their estimated Ca^{2+} EC_{50} (I). The Ca^{2+}-sensitive currents were normalized to the maximum Ca^{2+}-sensitive current.

One-way ANOVA: p values are 0.0002 for K428A(QA/EK/DR) and <0.0001 for E425A(QA/EK/DR), D879A(QA/EK/DR), and D884A(QA/EK/DR). Numbers in parentheses denote the number of individual recordings. Data are represented as means ± SEM.

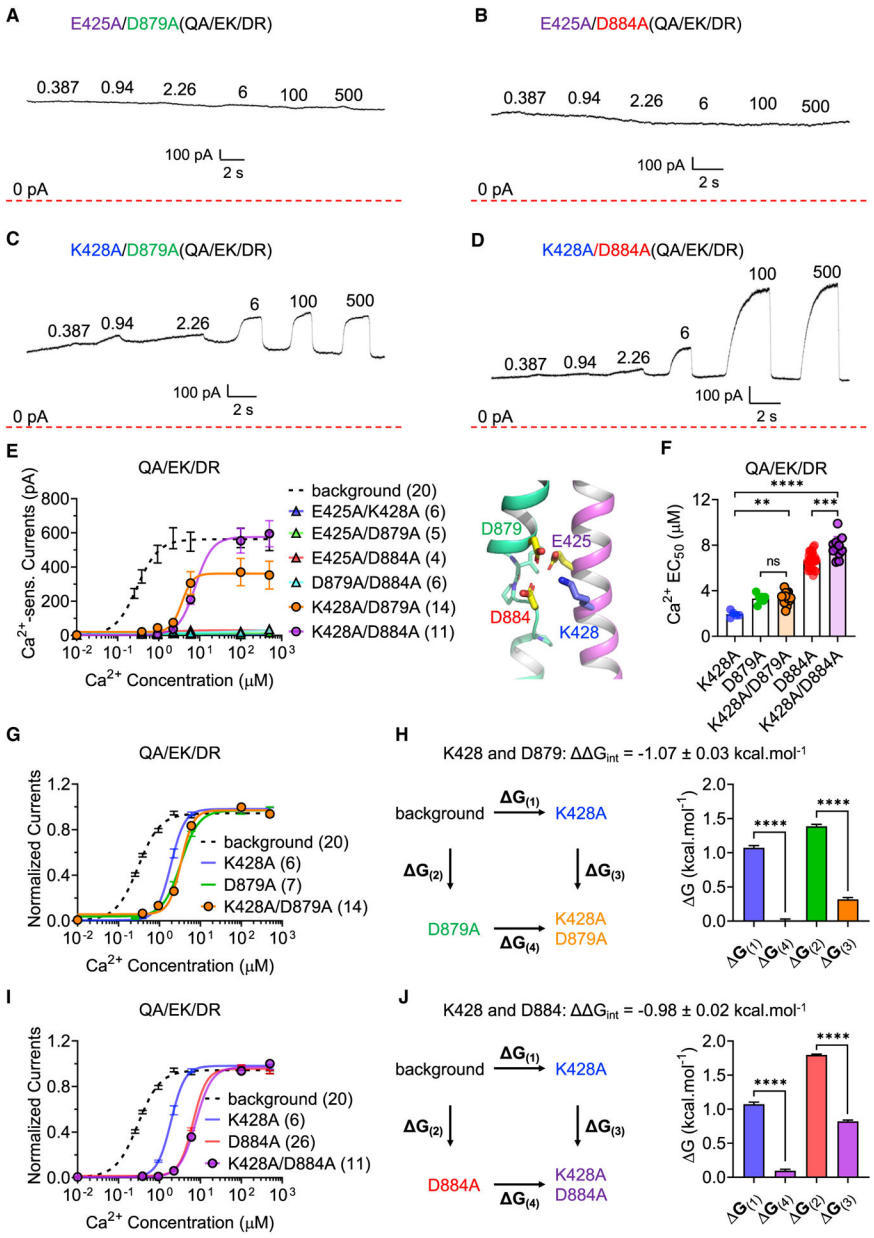

Figure 5. Differential Roles of the Third Ca^{2+} Site Residues in Ca^{2+} Binding

(A–D) Representative recordings of the QA/EK/DR background carrying an additional double mutation at the third Ca^{2+} site: E425A/D879A (A), E425A/D884A (B), K428A/D879A (C), and K428A/D884A (D). Ca^{2+} concentrations are shown as numbers above outward current deflections (in micromolar). The membrane was held at +60 mV. Red dashed line indicates 0-pA baseline.

(E and F) Quantifications of the Ca^{2+}-activated currents from double mutants at the third Ca^{2+} binding site on the QA/EK/DR background (E) and their estimated Ca^{2+} EC_{50} (F). Structure of the third Ca^{2+} site indicates the locations of the binding residues.

(G and I) Normalized Ca^{2+} dose-response curves from mutations of K428-D879 and K428-D884 pairs on the QA/EK/DR background.

(H and J) Double-mutant cycle analyses of K428-D879 and K428-D884 pairs. The free energy changes ($\Delta G_{(s)}$) were calculated to obtain the interaction energy: $\Delta\Delta G_{int} = \Delta G_{(4)} \Delta G_{(1)} = \Delta G_{(3)} \Delta G_{(2)}$. Background refers to the QA/EK/DR construct.
One-way ANOVA: in (F), p values are 0.0013 for K428A versus K428A/D879A, <0.0001 for K428A versus K428A/D884A, 0.9996 for D879A versus K428A/D879A, and 0.0001 for D884A versus K428A/D884A; in (H) and (J), p values are all <0.0001. Numbers in parentheses denote the number of individual recordings. Data are represented as means ± SEM.

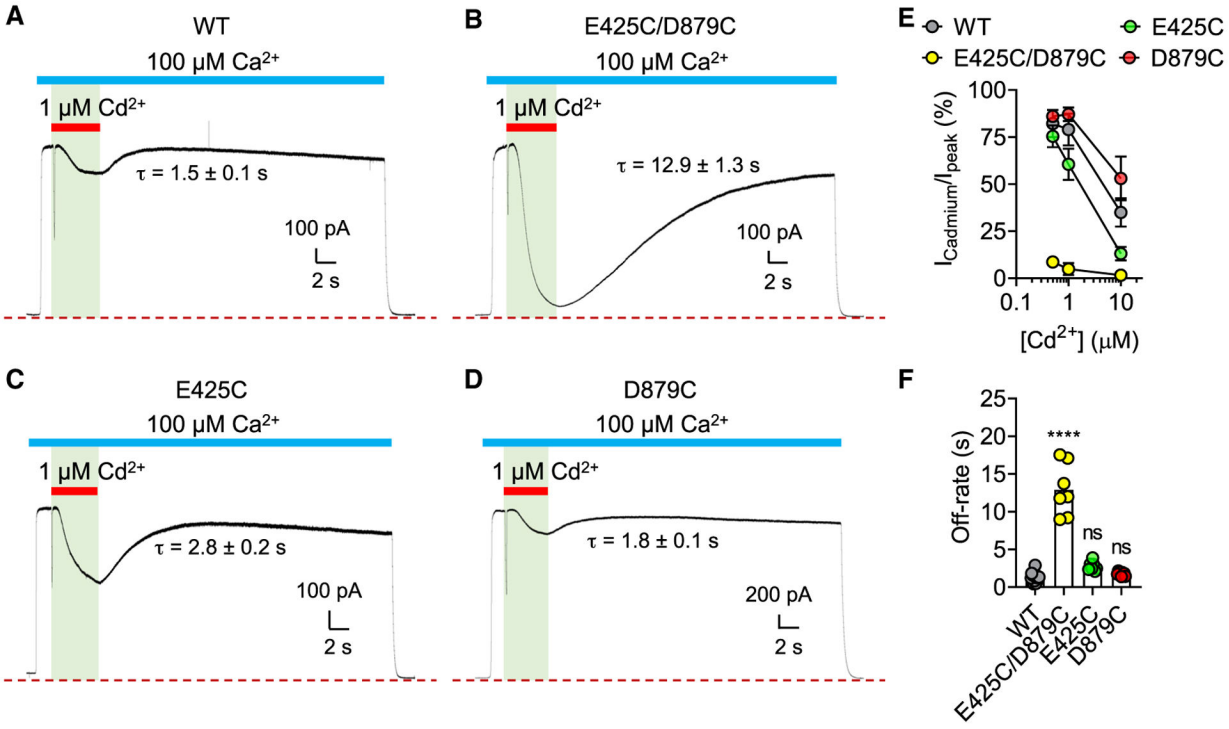

Figure 6. Cysteine-Mediated Stabilization of TM2-TM10 via Cd^{2+} Metal Bridging Inhibits TMEM16A Channel Activation

(A–D) Representative recordings indicating the effects of 1 μM Cd^{2+} on channel opening of TMEM16A WT (A), E425C/D879C (B), E425C (C), and D879C (D). The membrane was held at +60 mV. Red dashed line indicates 0-pA baseline.

(E) Quantifications of the dose-dependent Cd^{2+}-mediated inhibition of TMEM16A WT, E425C/D879C, E425C, and D879C. n = 4–25 recordings for each concentration of Cd^{2+}.

(F) Current recovery time constant (off-rate) of wild type (WT) and mutants after application of 1 μM Cd^{2+} in the presence of 100 μM Ca^{2+}. One-way ANOVA: p values are <0.0001, 0.1208, and 0.8519 for E425C/D879C, E425C, and D879C, respectively. Numbers in parentheses denote the number of individual recordings. Data are represented as means ± SEM.

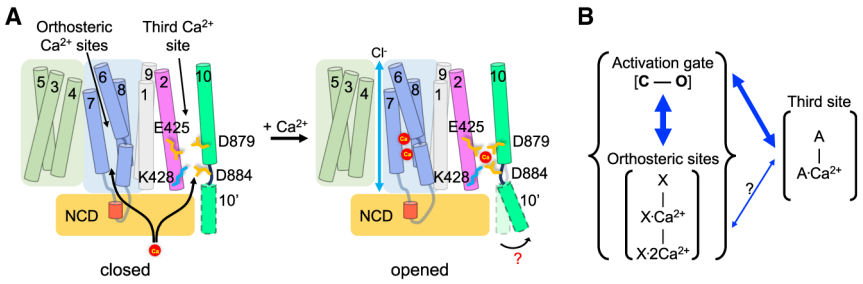

Figure 7. Proposed Mechanism of Allosteric Modulation via the Third Ca^{2+} Site

(A) A proposed allosteric gating mechanism shown in a TMEM16A topological model. Ca^{2+} binding to the orthosteric sites and the third Ca^{2+} site can activate and modulate TMEM16A activation gate through short-range and long-range allosteric coupling, respectively. Movement of TM10' is speculated based on the structural study of TMEM16K (Bushell et al., 2019).

(B) A simplified Ca^{2+}-dependent gating scheme of TMEM16A describing the relationships between the activation gate, the orthosteric Ca^{2+} binding sites, and the third Ca^{2+} site. Blue arrows represent allosteric coupling among the Ca^{2+} sensors and the activation gate.

KEY RESOURCES TABLE

REAGENT or RESOURCE	SOURCE	IDENTIFIER
Bacterial and Virus Strains		
Escherichia coli (MAX Efficiency DH5α competent cells)	Invitrogen	Cat#18258012
Chemicals, Peptides, and Recombinant Proteins		
Opti-MEM Reduced Serum Medium	GIBCO	Cat#11058021
Poly-L-lysine (PLL)	Sigma-Aldrich	Cat#P2636
Laminin	Sigma-Aldrich	Cat#L-2020
X-tremeGENE 9 DNA Transfection Reagent	Sigma-Aldrich	Cat#6365787001
Fura-2 pentapotassium salt	ATT Bioquest	Cat#21025
Critical Commercial Assays		
Calcium Calibration Buffer Kit	Biotum	Cat#59100
Experimental Models: Cell Lines		
Human Embryonic Kidney (HEK293T) cells	ATCC	RRID: CVCL_0045
Oligonucleotides		
Custom-designed primers for mutagenesis of mTMEM16A constructs (see Table S2)	IDT-DNA Technologies	N/A
Recombinant DNA		
TMEM16A-pEGFP-N1 from *Mus musculus*	(Tien et al., 2014)	N/A
mTMEM16A E425A	This paper	N/A
mTMEM16A K428A	This paper	N/A
mTMEM16A D879A	This paper	N/A
mTMEM16A D884A	This paper	N/A
mTMEM16A E425K	This paper	N/A
mTMEM16A K428E	This paper	N/A
mTMEM16A D879K	This paper	N/A
mTMEM16A D884K	This paper	N/A
mTMEM16A Q645A	(Peters et al., 2018)	N/A
mTMEM16A E425A/Q645A	This paper	N/A
mTMEM16A K428A/Q645A	This paper	N/A
mTMEM16A D879A/Q645A	This paper	N/A
mTMEM16A D884A/Q645A	This paper	N/A
mTMEM16A E425K/Q645A	This paper	N/A
mTMEM16A K428E/Q645A	This paper	N/A
mTMEM16A D879K/Q645A	This paper	N/A
mTMEM16A D884K/Q645A	This paper	N/A
mTMEM16A Q645A/E701K/D734R	This paper	N/A
mTMEM16A E425A/Q645A/E701K/D734R	This paper	N/A
mTMEM16A K428A/Q645A/E701K/D734R	This paper	N/A
mTMEM16A D879A/Q645A/E701K/D734R	This paper	N/A
mTMEM16A D884A/Q645A/E701K/D734R	This paper	N/A

REAGENT or RESOURCE	SOURCE	IDENTIFIER
mTMEM16A E425A/K428A/Q645A/E701K/D734R	This paper	N/A
mTMEM16A E425A/D879A/Q645A/E701K/D734R	This paper	N/A
mTMEM16A E425A/D884A/Q645A/E701K/D734R	This paper	N/A
mTMEM16A K428A/D879A/Q645A/E701K/D734R	This paper	N/A
mTMEM16A K428A/D884A/Q645A/E701K/D734R	This paper	N/A
mTMEM16A D879A/D884A/Q645A/E701K/D734R	This paper	N/A
mTMEM16A E425C	This paper	N/A
mTMEM16A K428C	This paper	N/A
mTMEM16A D879C	This paper	N/A
mTMEM16A D884C	This paper	N/A
mTMEM16A E425C/D879C	This paper	N/A
mTMEM16A E425C/D884C	This paper	N/A
mTMEM16A K428C/D879C	This paper	N/A
mTMEM16A K428C/D884C	This paper	N/A
mTMEM16A E425H/D879C	This paper	N/A
pCMV3-hPLSCR1-OFPSpark®	Sino Biological	Cat#HG16877-ACR
Software and Algorithms		
PyMOL	Schrödinger	https://pymol.org/2/
Axon PClamp 10 software	Molecular Devices	https://www.moleculardevices.com/
MATLAB	Mathworks	https://www.mathworks.com/products/matlab.html
Excel	Microsoft Office	N/A
Prism 8	GraphPad	https://www.graphpad.com/scientific-software/prism/
Illustrator	Adobe	https://www.adobe.com/products/illustrator.html
WEBMAXC (metal chelation prediction software)	Chris Patton, Stanford University	https://somapp.ucdmc.ucdavis.edu/pharmacology/bers/maxchelator/
Uniprot Sequence Alignment	UniProt	https://www.uniprot.org/align/